Available online at www.sciencedirect.com

SciVerse ScienceDirect

Journal of the European Ceramic Society 32 (2012) 2341–2349

www.elsevier.com/locate/jeurceramsoc

Role of oxygen pressure on the stability of lanthanum strontium manganite–yttria stabilized zirconia composite

Manoj K. Mahapatra, Sanjit Bhowmick, Na Li, Prabhakar Singh *

Center for Clean Energy Engineering, Department of Chemical, Materials and Biomolecular Engineering, University of Connecticut, Storrs, CT 06269, USA

Received 6 January 2012; received in revised form 29 February 2012; accepted 1 March 2012
Available online 27 March 2012

Abstract

We have investigated the structural and chemical stability of $La_{0.8}Sr_{0.2}MnO_3$ (LSM)–8 mol.% yttria stabilized zirconia (YSZ) composite. LSM and YSZ powders were mixed and sintered at 1400 °C for 10 h in controlled atmosphere ($PO_2 = 0.21$ to 10^{-6} atm). The unit cell volume of LSM increases during exposure to reduced oxygen partial pressure while it remains unchanged for YSZ. During reduction in the oxygen partial pressure from 0.21 atm to 10^{-6} atm, the solubility of manganese in YSZ increases from ∼10 at.% to ∼15 at.%. Lower oxygen partial pressure also results in the grain growth and formation of $La_2Zr_2O_7$ and MnO_x (Mn_3O_4) compounds lowering the stability of the LSM–YSZ composite. On subsequent sintering in 0.21 atm PO_2, the $La_2Zr_2O_7$ and MnO_x compounds tend to disappear indicating the reversibility of the interaction. The reversibility of LSM–YSZ reaction has been independently confirmed using $La_2Zr_2O_7$ and MnO_x.

Keywords: Fuel cells; Perovskites: ZrO_2; Sintering; Lanthanum zirconate

1. Introduction

Solid oxide fuel cell (SOFC) is one of the most attractive electrochemical devices to convert chemical energy into electrical energy.[1–3] For practical applications, SOFCs should demonstrate a lifetime of ∼5000 h for mobile applications and ∼40,000 h for stationary applications under the nominal operating conditions (650–1000 °C and exposure to oxidizing and reducing atmospheres).[1–4] While the efficiency of SOFCs can be increased to more than 50% by exploiting new materials and designs, the performance degradation with time remains one of the major challenges.[5] Instability of bulk materials, surface poisoning and interface separation at the cell and stack level (cathode, electrolyte, anode, interconnect, and gas seal) during cell fabrication and operation contribute to the electrical performance degradation.[4,6]

Strontium doped lanthanum manganite (LSM), 8 mol.% yttrium doped zirconia (YSZ), and nickel–YSZ cermet have been widely investigated for use as SOFC cathode, electrolyte, and anode components, respectively.[2] These materials meet the primary requirements of high electrical conductivity of the cathode (∼200 S/cm), high ionic conductivity of the electrolyte (∼0.01 S/cm), and matched thermal expansion coefficient (CTE, $10.8–11.8 \times 10^{-6}$/°C) under the nominal cell operating conditions.[1–4] In order to improve the SOFC performance, mixed ionic electronic conductors (MIECs) as cathode materials have also been investigated.[7,8] Strontium doped lanthanum ferrite, cobaltite, and cobaltite ferrite are some of the examples of MIECs. These materials show high electrical and ionic conductivity as well as electrocatalytic activity for the oxygen reduction. Higher CTE ($12.2–20.5 \times 10^{-6}$/°C) of these materials, however, make them prone to cracking and delamination from the adjoining interfaces (electrolyte and contact layers) during SOFC operation resulting in the performance degradation.[7,9] It is also noted that the above properties of these materials vary with temperature and the chemical stability remains poor. For example, the conductivity of LSF ($La_{0.5}Sr_{0.5}FeO_3$) decreases from 352 S/cm at 550 °C to ∼180 S/cm at 900 °C. LSF also reacts with YSZ above 800 °C to form an insulating strontium zirconate ($SrZrO_3$) phase at the electrode–electrolyte interface.[8,10] The conductivity of LSCF ($La_{0.6}Sr_{0.4}Co_{0.2}Fe_{0.8}O_3$) decreases from ∼325 S/cm at 550 °C to ∼275 S/cm at 800 °C.[11] LSCF ($La_{0.6}Sr_{0.4}Co_{1-y}Fe_yO_{3-\delta}$) compounds decompose to A_2BO_4 and CoO at 600 °C and

---

* Corresponding author.
E-mail address: singh@engr.uconn.edu (P. Singh).

0955-2219/$ – see front matter © 2012 Elsevier Ltd. All rights reserved.
doi:10.1016/j.jeurceramsoc.2012.03.003

10^{-9} atm PO_2 and at 800 °C at 10^{-6} atm PO_2 for $y \leq 0.4$ and 10^{-21} atm at 600 °C and 10^{-15} atm at 800 °C for $y = 0.8$.[12] Despite the lower ionic conductivity (5.97×10^{-7} S/cm), LSM is preferred as a cathode material for its superior chemical stability and matched CTE with YSZ when compared to those of the MIECs.[8,13–15] The ionic conductivity and electro-catalytic activity of LSM cathode has been improved by increasing the electrochemically active sites (triple phase boundary length) incorporating YSZ in the composite form.[16] The reactions between LSM and YSZ at elevated temperatures (cell fabrication and cell operation) result in the formation of insulating lanthanum zirconate ($La_2Zr_2O_7$) and strontium zirconate ($SrZrO_3$) phases at the LSM–YSZ interface.[13,17,18] The conductivity of the $La_2Zr_2O_7$ and $SrZrO_3$ phases are in the range of 10^{-4}–10^{-5} S/cm which is much lower than those of LSM and YSZ resulting in an increase in cell resistance.[13,19]

The reaction between LSM and YSZ has been found to be predominantly dependent on the composition (Sr concentration and A/B ratio), surface area of the starting powders, sintering temperature, exposure time, and atmosphere.[17,19–25] At a dopant level below 30 mol.% strontium on the lanthanum site of LSM favors $La_2Zr_2O_7$ phase formation but dopant level of more than 30 mol.% strontium leads to $SrZrO_3$ phase formation.[20,26] Lowering of the A/B ratio in LSM may retard the formation of zirconate phases but cannot hinder the reaction.[20,23] A-site deficient LSM enhances densification and decreases the catalytic activity.[24,25] A wide range of temperature (1100–1400 °C) for the formation of zirconate phases have been reported.[17,20,23,26–29] The difference in the zirconate formation temperature is attributed to the composition and surface area of the starting LSM powders. The amount of zirconate phase increases with sintering time in all cases.[17,20,23,29] Reduction of oxygen partial pressure during sintering accelerates the zirconate phase formation.[22] For example, zirconate phases are absent when LSM–YSZ composite sintered in air at 1000 °C for 5 weeks but present while sintered in N_2 atmosphere.[22]

Although the exposure atmosphere on the microstructural and chemical stability of LSM–YSZ composite is important for the SOFC fabrication and operation, limited information exists in literature.[22] Localized distribution in the current density during cell and stack operation can also lead to changes in the localized oxygen partial pressure at the LSM–YSZ interface due to (1) temperature gradient and hot spot, (2) changes in the component microstructure, (3) the specific resistance of LSM and YSZ, and (4) variability in the repeat cell unit contact resistance in the stack.[27,28]This paper describes the role of oxygen pressure on microstructural evolution, reaction kinetics and interaction of LSM–YSZ composite.

2. Experimental procedure

2.1. Sample preparation

LSM ($La_{0.8}Sr_{0.2}MnO_3$, surface area 4.66 m^2/g, Fuelcell Materials, OH), YSZ (surface area 4.7 m^2/g), and carbon black (density 1.8 g/cm^3, CABOT Corporation, MA) powders in 1:1:0.12 mass ratio were ball milled for 24 h using ZrO_2 balls and ethanol. The mixed powder batch was dried for 24 h and pressed into pellets. Carbon black powder serves as pore former to obtain ~30 vol.% pores in the sample after bisque firing. The LSM–YSZ pellets were bisque fired in air at 1000 °C for 2 h in order to burn out carbon. Bulk porosity allows the samples to achieve uniform exposure to the controlled gas atmosphere.

The bisque fired samples were subsequently sintered at 1400 °C for 10 h in flowing dry air (PO_2 ~0.21 atm), N_2–1000 ppm O_2 (PO_2 ~10^{-3} atm), and N_2–1 ppm O_2 (PO_2 ~10^{-6} atm) in a tube furnace (Model No. 0300334, CM Inc., NJ) at a nominal flow rate of 20 sccm. Certified gas compositions (Airgas, North Haven, CT) were used in all the sintering experiments. Selected samples initially sintered in N_2–1000 ppm O_2 and N_2–1 ppm O_2 atmospheres, were resintered at 1400 °C for 10 h in dry air. For all the sintering experiments, the heating and cooling rates were 3 °C/min.

2.2. Characterization

The bulk density of the sintered LSM–YSZ samples was measured by Archimedes method following ASTM C20-97 standard. The density of at least five samples for each sintering atmospheres were measured. Average density is reported.

X-ray diffraction (XRD) studies, using a Bruker D8 Advance diffractometer (Bruker AXS Inc., Madison, WI) were carried out to identify the structure and phases present in the sintered LSM–YSZ composite. The scan step was 0.04° with CuK_α radiation ($\lambda = 1.5406$ Å).

The LSM–YSZ samples were polished to optical finish. The polished samples were cleaned in an ultrasonic bath with water and dried and wiped with ethanol. The microstructures of the polished samples were examined using scanning electron microscope (SEM, Quanta 600, FEI Company, Hillsboro, OR). The EDS module attached to the SEM was used to analyze the elemental composition of various phases in the sintered samples. A minimum of ten EDS spot analysis was carried out for each phase. The average elemental composition is reported.

The TEM and STEM specimens described in this paper were prepared using a focused ion beam (FIB) instrument (FEI strata 400S, FEI Company, Hillsboro, OR, 30 keV Ga^+ ions) with a dual-beam column, combining a scanning electron beam and an ion beam in one unit. The dual beam allows high-resolution imaging of the surface of the sample during the ion-beam milling process. An Omniprobe nanomanipulator (Omniprobe Auto Probe^{TM} 200) is used for the in situ TEM specimen lift-out technique. For the current study, a sample thickness between 75 and 100 nm provides suitable results. TEM studies and STEM-XEDS line scans were performed using Tecnai T12 TEM. In STEM-XEDS line scan, a series of spectra were acquired while the beam was scanning along a defined line. The elemental distribution profiles were obtained by selecting the energy windows of a particular element.

Table 1
Bulk density and theoretical density of the LSM–YSZ composites sintered in different atmospheres.

Sintering atmosphere	Density (g/cm^3)	Theoretical density (%)
Air	5.86 ± 0.04	94
N_2–1000 ppm O_2	5.83 ± 0.08	94
N_2–1 ppm O_2	5.77 ± 0.09	93
N_2–1000 ppm O_2 followed by air	5.97 ± 0.04	95
N_2–1 ppm O_2 followed by air	5.88 ± 0.09	94

3. Results

3.1. Density

The average density of the sintered samples is listed in Table 1. 93–95% theoretical density is obtained for the LSM–YSZ composites. Slight decrease in the density is observed with decreasing oxygen partial pressure. At high theoretical density, the effect of PO_2 on the densification is not significant.

3.2. Phase evolution

The role of sintering atmosphere on the compound formation and structural changes in the LSM–YSZ composites, as identified by XRD, is shown in Fig. 1. Cubic zirconia (JCPDS number: 00-030-1468) is observed for all the samples regardless of sintering atmosphere. Rhombohedral LSM (JCPDS number: 00-053-0058) is observed for the samples sintered in air. Rhombohedral (JCPDS number: 00-074-8264) LSM, cubic $La_2Zr_2O_7$ (JCPDS number: 00-017-0450), and MnO_x (Mn_3O_4 JCPDS number: 00-024-0734) phases are found for the samples sintered in 10^{-3} atm and 10^{-6} atm PO_2. Although rhombohedral LSM is observed for the samples sintered in 10^{-3} atm and 10^{-6} atm PO_2, the shift in XRD pattern indicates that the lattice parameters are different from that of air sintered samples leading to higher unit cell volume as shown in Fig. 2. The samples sintered in 10^{-3} atm and 10^{-6} atm PO_2 followed by air atmosphere sintering show identical XRD peak positions and intensity to those of air sintered samples indicating identical phase formation. The unit cell volume, after resintering, decreases as shown in Fig. 2. These observations indicate that sintering atmosphere significantly influences the phase evolution and the structure of LSM. The reaction between LSM and YSZ is also found reversible as a function of PO_2.

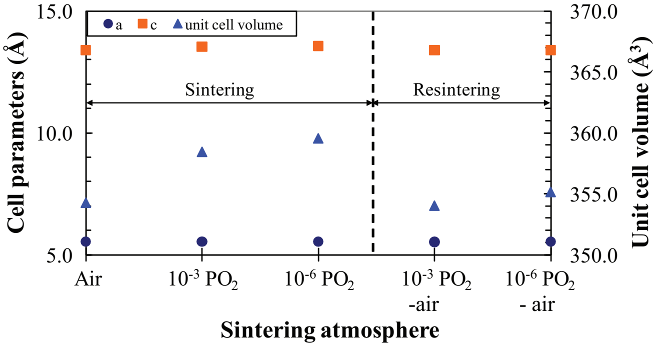

Fig. 2. Lattice parameters and unit cell volume of LSM in LSM–YSZ composites sintered in different sintering atmospheres.

3.3. Microstructure and chemical composition

The microstructure of the polished LSM–YSZ composites sintered in different atmospheres is shown in Fig. 3. For the sample sintered in air (Fig. 3a), both LSM and YSZ are homogeneously distributed. The grain size of these phases varies from 1.5 μm to 6 μm. The dark phases are YSZ (marked as 1) and bright phases are LSM (marked as 2) as confirmed by EDS analysis given in Table 2. However, Y and O are not considered in the EDS elemental analysis. The X-ray energies of Y and Zr are very close and could not be distinguished. The atomic number of oxygen is low for reliable quantitative analysis. The EDS analyses show the presence of ∼7 at.% La and ∼10 at.% Mn in the YSZ.

For the samples sintered in 10^{-3} atm PO_2, four distinct phases are observed (Fig. 3b). The dark phase (marked as 1) is YSZ, gray colored phase (marked as 2) is LSM, the brighter phase

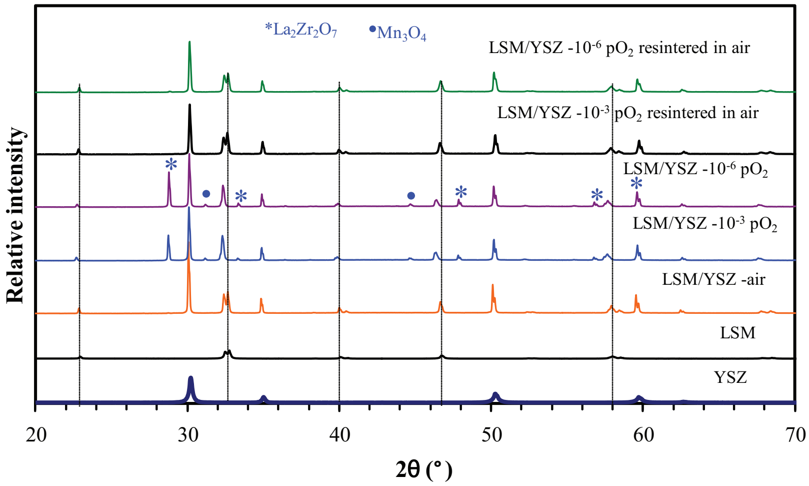

Fig. 1. XRD patterns of the LSM–YSZ composites in different sintering atmospheres. Dotted lines show the shift in 2θ position for LSM with sintering atmosphere.

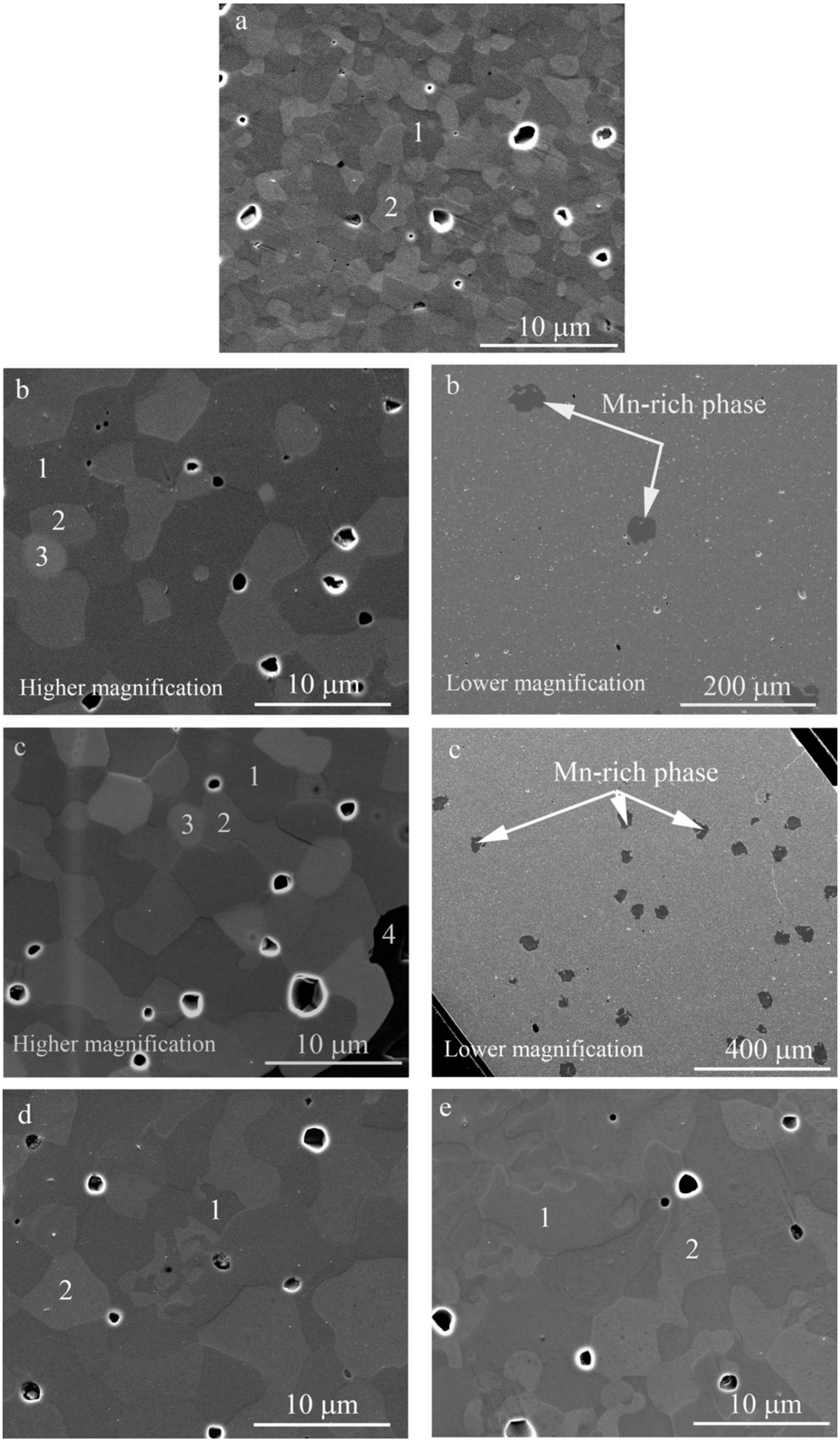

Fig. 3. SE images of the polished LSM–YSZ composites sintered at 1400 °C for 10 h in: (a) air, (b) N_2–1000 ppm O_2, (c) N_2–1 ppm O_2, (d) initially sintered in N_2–1000 ppm O_2 and resintered in air, and (e) initially sintered in N_2–1 ppm O_2 and resintered in air. Low magnification images in (b) and (c) show the presence of Mn-rich phases in the bulk sample.

Table 2
SEM-EDS analysis of LSM–YSZ composites sintered in different atmospheres (as shown in Fig. 3).

Sintering atmosphere	Elements				Compounds
	La	Sr	Mn	Zr	
Air					
1	6.5 ± 1.0		9.5 ± 1.1	84.0 ± 1.7	Solid solution ZrO_2 with La and Mn
2	42.3 ± 0.9	12.5 ± 0.4	45.1 ± 0.9		LSM
N_2–1000 ppm O_2					
1	6.7 ± 0.4		13.8 ± 0.3	79.4 ± 0.5	Solid solution ZrO_2 with La and Mn
2	39.4 ± 0.3	14.3 ± 0.4	42.2 ± 0.8	4.1 ± 0.7	LSM
3	43.8 ± 0.5			55.7 ± 0.5	$La_2Zr_2O_7$
N_2–1 ppm O_2					
1	7.5 ± 0.6		15.0 ± 0.8	77.6 ± 1.3	Solid solution ZrO_2 with La and Mn
2	41.5 ± 1.1	13.2 ± 0.5	42.5 ± 1	2.8 ± 1.0	LSM
3	45.9 ± 0.1			54.1 ± 0.1	$La_2Zr_2O_7$
N_2–1000 ppm O_2 followed by air					
1	7.0 ± 0.4		10.3 ± 1.0	82.7 ± 1.0	Solid solution ZrO_2 with La and Mn
2	40.4 ± 0.3	13.8 ± 0.4	45.4 ± 0.4		LSM
3	39.1 ± 0.6	14.2 ± 0.5	43.3 ± 0.6	3.3 ± 0.7	LSM
N_2–1 ppm O_2 followed by air					
1	5.8 ± 1.0		12.0 ± 1.1	82.1 ± 1.4	Solid solution ZrO_2 with La and Mn
2	41.9 ± 2.2	11.7 ± 1.6	44.0 ± 1.9	2.4 ± 2.5	LSM

(marked as 3) is $La_2Zr_2O_7$ and the darkest phase (marked in low magnification image in Fig. 3b) is MnO_x as confirmed by EDS analysis (Table 2). The LSM and YSZ are homogeneously distributed. MnO_x phase (~30 μm, Mn_3O_4 as confirmed by XRD) is randomly distributed (Fig. 3b). The grain sizes of LSM, YSZ, and $La_2Zr_2O_7$ vary from 2 to 4 μm, 5 to 10 μm, and 1 to 3 μm, respectively. The EDS analyses show the presence of ~7 at.% La and ~14 at.% Mn in the YSZ and ~4.5 at.% Zr in the LSM.

For the sample sintered in 10^{-6} atm PO_2, four distinct phases are observed (Fig. 3c). The dark phase (marked as 1) is YSZ, the gray colored phase (marked as 2) is LSM, the brighter phase (marked as 3) is $La_2Zr_2O_7$ and the darkest phase (marked as 4) is MnO_x as confirmed by EDS spot analyses (Table 2). The LSM and YSZ are homogeneously distributed. MnO_x phase of ~30 μm in size (Mn_3O_4 as confirmed by XRD) is randomly distributed (Fig. 3c). The grain sizes of LSM, YSZ, and $La_2Zr_2O_7$ vary from 4 to 6 μm. The EDS analyses show the presence of ~7.5 at.% La and ~15 at.% Mn in the YSZ and ~3 at.% Zr in the LSM.

For the sample initially sintered in 10^{-3} atm PO_2 and resintered in air, significant morphological changes are observed. The dark phase is YSZ (marked as 1 in Fig. 3d) and the bright phase is LSM (marked as 2 in Fig. 3d). The grain size of the LSM and YSZ phases vary from 1 to 8 μm. Overall, the YSZ grains are larger than LSM. The EDS analyses show the presence of ~7 at.% La and ~10 at.% Mn in the YSZ and ~4 at.% Zr in some of the LSM grains.

For the samples initially sintered in 10^{-6} atm PO_2 and resintered in air, significant morphological changes are observed. The dark phase is YSZ (marked as 1 in Fig. 3e) and the bright phase is LSM (marked as 2 in Fig. 3e). The grain size of the LSM and YSZ phases vary from 1 to 8 μm. Overall, the YSZ grains are larger than LSM. The EDS analyses show that ~7 at.% La and ~12 at.% Mn diffuse into the YSZ. 3–4 at.% Zr from YSZ also diffuses into some of the LSM grains.

Above observations indicate that the sintering atmosphere affects the microstructural changes and the interaction between LSM and YSZ. The overall grain sizes of the LSM and YSZ phases are larger for the samples sintered in 10^{-3} atm and 10^{-6} atm PO_2 when compared to air sintered samples. The grain sizes of the LSM and YSZ for the samples initially sintered in 10^{-3} atm and 10^{-6} atm PO_2 and resintered in air vary considerably and an average grain size increases further. Regardless of sintering atmospheres, ~7 at.% La and 10–15 at.% Mn are present in the YSZ. The amount of Mn in YSZ is higher (14–15 at.%) for the samples sintered in 10^{-3} atm and 10^{-6} atm PO_2 but decreases to 10–12 at.% on further sintering in air. For all the samples except the sample sintered in air, 2.5–5 at.% Zr is observed in the LSM phases. For the sample sintered in air, no secondary phases are formed. $La_2Zr_2O_7$ and Mn_3O_4 phases evolve for the samples sintered in 10^{-3} atm and 10^{-6} atm PO_2 atmospheres. The amounts of these phases are found to be higher for the samples sintered in 10^{-6} atm PO_2 as evident from the microstructures in Fig. 3b and c and also supported by the higher intensity of the $La_2Zr_2O_7$ and Mn_3O_4 phases in the XRD plots (Fig. 1). This infers that the extent of reaction between LSM and YSZ increases with decreasing oxygen partial pressure in the sintering atmospheres. On subsequent resintering of these samples in air, the $La_2Zr_2O_7$ and Mn_3O_4 compounds disappear which is consistent with the XRD results. The results indicate that the reaction between the LSM and YSZ is reversible.

The TEM images of the selected LSM–YSZ composites sintered in different atmospheres are shown in Figs. 4–6. While Fig. 4 represents air sintered sample, Figs. 5 and 6 represent the samples initially sintered in 10^{-6} PO_2 and 10^{-6} PO_2 and resintered in air, respectively. Because of better spatial resolution and lower sampling volume, TEM provides detailed morphological and compositional changes in the samples. For the sample sintered in air (Fig. 4), it has been observed that two phases are homogeneously distributed. The phases are identified as LSM

Table 3
TEM-EDS analysis of LSM–YSZ composites sintered in different atmospheres (as shown in Figs. 4–6).

Sintering atmosphere	Elements					Compounds
	La	Sr	Mn	Zr	Y	
Air						
1	1.3 ± 0.2		4.4 ± 0.3	82.7 ± 0.8	12.2 ± 0.5	Solid solution ZrO_2 with La and Mn
2	5.2		4.9	79.0	10.9	Solid solution ZrO_2 with La and Mn
3	35.2 ± 1.4	14.1 ± 1.2	50.5 ± 1.4			LSM
4	31	17.3	50.1	2.7		LSM
5	46.1	10.8	43.0			LSM
6	33.6	14.4	50.7		1.3	LSM
N_2–1 ppm O_2						
1	34.0	13.1	48.9	4.0		LSM
2	21.1	14.2	61.0	3.5		LSM
3	2.7 ± 1.0	0.6 ± 0.3	9.5 ± 0.7	76.8 ± 1.1	11.5 ± 1.0	Solid solution ZrO_2 with La and Mn
4	28.3	0.6	0.5	67.9	2.9	$La_2Zr_2O_7$ and ZrO_2
5	1.8 ± 1.0	0.2 ± 0.1	98.3 ± 1.2	1.1 ± 0.5		MnO_x
N_2–1 ppm O_2 followed by air						
1	31.3			68.7		$La_2Zr_2O_7$ and ZrO_2
2	50.4			41	8.52	$La_2Zr_2O_7$
3	1.9		3.7 ± 0.8	84.8 ± 3.2	11.4 ± 2.5	Solid solution ZrO_2 with La and Mn
4	5.8		8.2	72.9	13.0	Solid solution ZrO_2 with La and Mn
5	44.3	11.2	44.5	14.1		LSM and ZrO2
6	24.5	18.2	57.3			LSM

and YSZ from the STEM-XEDS analysis given in Table 3. The grain sizes are 1–6 µm, consistent with SEM. Submicron sized grains are observed (marked as 3 and 6 in Fig. 4). Twins are also observed in the LSM grains. The compositions of the LSM and YSZ phases vary from grain to grain. 2–4 at.% La and 4–5 at.% Mn are present in the YSZ (marked as 1 and 2 in Fig. 4). Similarly, the LSM grains contain 30–46 at.% La, 11–17 at.% Sr, and 43–51 at.% Mn as given in Table 3. STEM-XEDS line scan analysis was carried out along YSZ grain in-between two LSM grains (marked as A_1–A_2 line in Fig. 4). No secondary phase has been found at the LSM and YSZ grain boundaries. For brevity, concentration profiles of the elements are not shown.

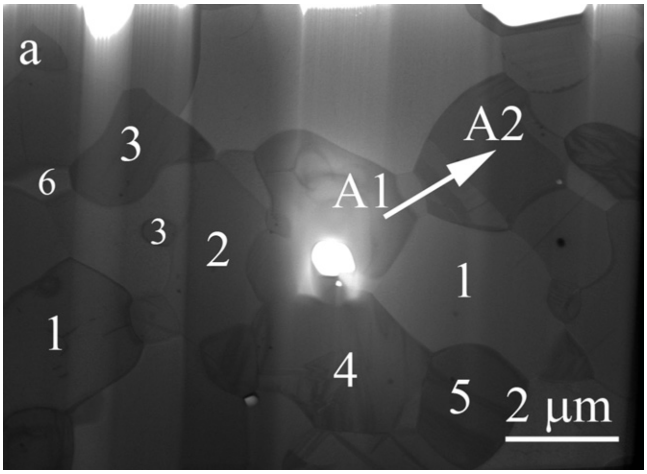

Fig. 4. TEM image of the LSM–YSZ composite sintered at 1400 °C for 10 h in air. The concentration profiles of elements are determined along the line A_1–A_2 in the TEM image.

For the sample sintered in 10^{-6} atm PO_2 (Fig. 5a), four different phases are observed. From the EDS analysis in Table 3, the phases are identified as LSM (marked as 1 and 2), YSZ (marked as 3), $La_2Zr_2O_7$ (marked as 4), and MnO_x (marked as 5). The MnO_x grain is elongated and oriented in a layer form. Due to the non-uniform distribution of these phases, the grain sizes could not be determined. The LSM composition varies from grain to grain. 3 at.% La and 10 at.% Mn are present in the YSZ. 4 at.% Zr is found in some of the LSM grains. No secondary phase has been found at the LSM and YSZ grain boundaries, consistent with the concentration profiles of the La, Sr, Mn, Y, and Zr at the grain boundary (Fig. 5b).

For the sample initially sintered in 10^{-6} atm PO_2 and resintered in air (Fig. 6), three different phases are observed. From the EDS analysis in Table 3, the phases are identified as $La_2Zr_2O_7$ (marked as 1,2), YSZ (marked as 3,4), and LSM (marked as 5,6). The grain sizes of these phases are 1–5 µm. Twins are observed in the LSM grains. The compositions of the LSM and YSZ vary from grain to grain. 2–6 at.% La and 4–8 at.% Mn are found in the YSZ. No secondary phase has been found at the LSM and YSZ grain boundaries, consistent with the elemental concentration profiles at grain boundary.

The TEM analysis, in all cases, shows the presence of twins in LSM grains and layered morphology of MnO_x phase and reveals that the LSM, YSZ, and $La_2Zr_2O_7$ grain compositions vary from grain to grain. The absence of MnO_x phase in the sample initially sintered in 10^{-6} atm PO_2 and resintered in air indicates that the reaction between LSM and YSZ is reversible, consistent with the XRD and SEM analysis. However, presence of the $La_2Zr_2O_7$ grains in the sample initially sintered in 10^{-6} atm PO_2 and resintered in air suggests that the complete reversibility of the reaction has not been attained within the experimental conditions.

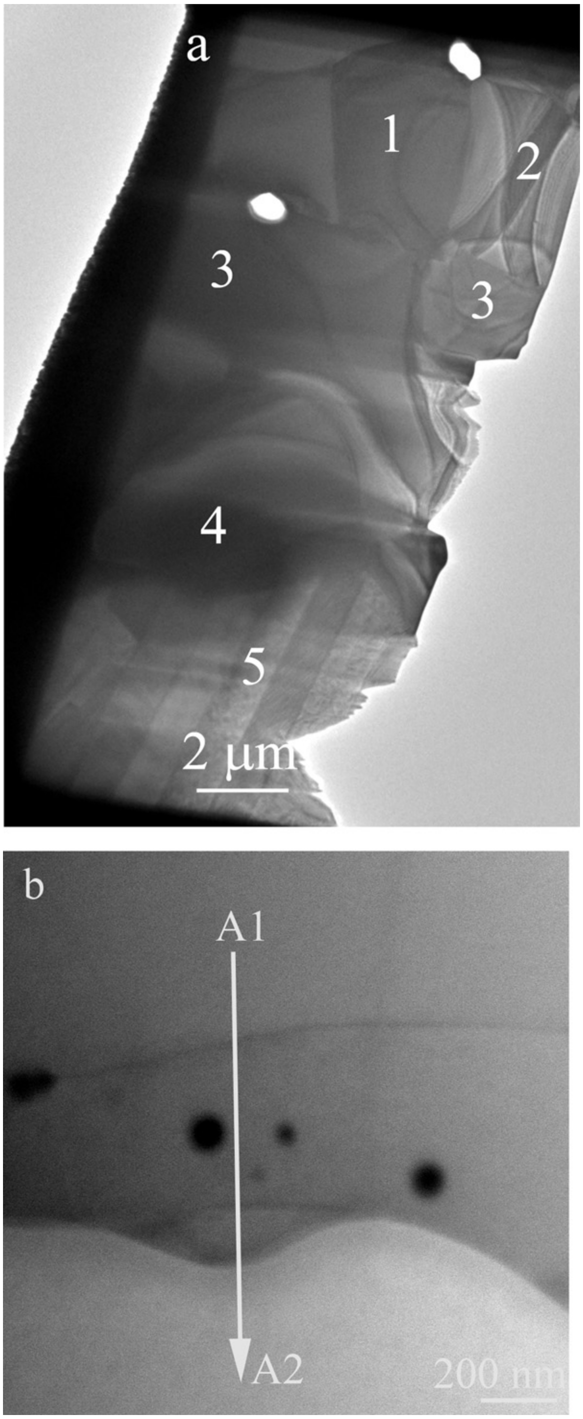

Fig. 5. (a) Low and (b) high magnification TEM images of the LSM–YSZ composite sintered at 1400 °C for 10 h in N_2–1 ppm O_2 environment. The concentration profiles of elements are determined along the line A_1–A_2 in the TEM image (b).

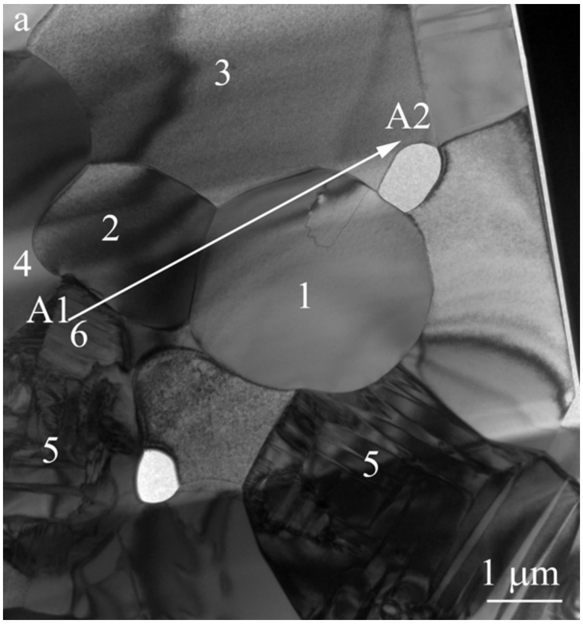

Fig. 6. TEM image of the LSM–YSZ composite resintered in air at 1400 °C for 10 h of the sample initially sintered in N_2–1 ppm O_2. The concentration profiles of elements are determined along the line A_1–A_2 in the TEM image.

3.4. Reversible reaction

To check the reversibility of the LSM–YSZ reaction with respect to oxygen partial pressure, $La_2Zr_2O_7$ compound was first prepared. The YSZ and La_2O_3 powders were mixed and calcined at 1300 °C for 24 h. The calcined powder was crushed into fine powders and pressed into pellets. The pellets were sintered at 1500 °C for 24 h. From the XRD pattern of the sintered samples in Fig. 7, formation of the $La_2Zr_2O_7$ (JCPDS number 01-070-5602) phase is confirmed. $Y_2Zr_2O_7$ (JCPDS number 01-074-9311) and trace amount of unreacted La_2O_3 (JCPDS number 01-071-5408) phases were also observed.

The prepared $La_2Zr_2O_7$ samples were crushed into fine powders and mixed with MnO_2 powder (1:2 mole ratio). The mixed powder was pressed into pellets and sintered at 1400 °C for 10 h in air. The XRD pattern in Fig. 7 shows rhombohedral $LaMnO_3$ (JCPDS number 01-070-3942), cubic YSZ (JCPDS number 01-077-2112), and small amount of $La_2Zr_2O_7$ and Mn_3O_4 phases. Large reduction in the amount of $La_2Zr_2O_7$ suggests that the $La_2Zr_2O_7$ phase reacts with MnO_2 and forms $LaMnO_3$ and YSZ. The absence of the $Y_2Zr_2O_7$ phase indicates that it also reacts with MnO_2 to form $LaMnO_3$ and YSZ. These observations confirm that the reaction between (a) LSM and YSZ results in $La_2Zr_2O_7$ and MnO_x and (b) the $La_2Zr_2O_7$ and MnO_x results

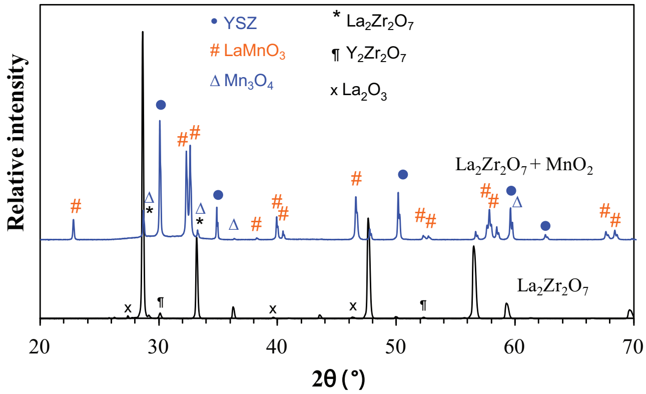

Fig. 7. XRD patterns of the sintered $La_2Zr_2O_7$ and the mixture of $La_2Zr_2O_7$ powder with MnO_2 after sintering at 1400 °C for 10 h in air.

in $LaMnO_3$ and ZrO_2 formation. Unreacted MnO_2 transforms into the more stable Mn_3O_4 phase during sintering.

4. Discussion

The effect of sintering atmosphere on the stability of LSM–YSZ composite will be discussed from several aspects: structural and morphological changes, reaction kinetics, and the reversibility of the reaction between LSM and YSZ.

Respective phase formation during the sintering in various gas atmospheres is shown in Tables 2 and 3. Mn ions diffuse readily in YSZ due to its smaller ionic radii and highest diffusivity among lanthanum and strontium ions.[29,30] The change in the lattice parameters of LSM structure is explained based on the changes in the valence state of manganese ions (Mn^{4+} to Mn^{3+}). In 10^{-3} atm and 10^{-6} atm PO_2, manganese ions reduce to lower valence state according to

$$2{\rm Mn}_{\rm Mn}{}^{\bullet} + {\rm O}_o^x = \frac{1}{2}{\rm O}_2 + V_o{}^{\bullet\bullet} + 2{\rm Mn}_{\rm Mn}^x \tag{1}$$

$$2{\rm Mn}_{\rm Mn}^x + {\rm O}_o^x = \frac{1}{2}{\rm O}_2 + V_o{}^{\bullet\bullet} + 2{\rm Mn}_{\rm Mn}^{/} \tag{2}$$

where $V_o{}^{\bullet\bullet}$, ${\rm Mn}_{\rm Mn}{}^{\bullet}$, ${\rm Mn}_{\rm Mn}^x$, and ${\rm Mn}_{\rm Mn}^{/}$ are oxygen vacancy, Mn^{4+}, Mn^{3+}, and Mn^{2+}, respectively. Reduction of Mn^{4+} and Mn^{3+} ions to larger Mn^{2+} ions increases the unit cell volume of the LSM.[31] Leading to the changes in LSM lattice parameters as indicated by peak shifts in the XRD pattern during sintering in 10^{-3} atm and 10^{-6} atm PO_2. As the Mn^{2+} ion is more soluble into the YSZ than Mn^{3+} and Mn^{4+} ions due to the favorable ionic radii, the concentration of manganese ion in the YSZ is the highest for the samples sintered in 10^{-6} atm PO_2.[32] Further sintering in air ($PO_2 = 0.21$ atm) oxidizes the Mn^{2+} ions into the Mn^{3+} ions. As a result, the solubility of manganese ions into the YSZ decreases as supported by the EDS spot analyses presented in Tables 2 and 3. The corresponding unit cell volume of the LSM also decreases (Fig. 2) to those of air sintered samples.

The overall grain size of the LSM–YSZ composites sintered in 10^{-3} atm and 10^{-6} atm PO_2 is larger than those for the samples sintered in air. At lower PO_2, oxygen vacancies increase due to change in the oxidation state of manganese ions as stated above (reactions (1) and (2)). Also the oxygen vacancies increase according to

$${\rm O}_o^x = V_o{}^{\bullet\bullet} + 2e + \frac{1}{2}{\rm O}_2 \tag{3}$$

The charge neutrality in the LSM is maintained through the stoichiometry and generation of cationic defects. The Mn^{4+} and Mn^{3+} ions accept the electrons from reaction (3) and reduced to Mn^{3+} and Mn^{2+} ions. The oxygen vacancies enhance the atomic mobility to the grain boundaries and free surfaces causing larger grain sizes. According to defect cluster model, the oxygen vacancies form ${\rm Mn}_{\rm Mn}^{/} - V_o{}^{\bullet\bullet} - {\rm Mn}_{\rm Mn}^{/}$ cluster.[33] It is postulated that the mobility of ${\rm Mn}_{\rm Mn}^{/} - V_o{}^{\bullet\bullet} - {\rm Mn}_{\rm Mn}^{/}$ cluster is the slowest and rate limiting step to enhance the LSM grain growth. Although YSZ is stable at 10^{-3} atm and 10^{-6} atm PO_2, presence of Mn^{2+} ion in the YSZ lattice creates additional oxygen vacancies which enhance the sintering and grain growth of YSZ.[18] For the samples initially sintered in 10^{-3} atm and 10^{-6} atm PO_2 and resintered in air, the further increase in grain size is likely due to the longer sintering time.

Thermochemical stability and formation of $La_2Zr_2O_7$ phase due to the reaction between LSM and YSZ is influenced by the temperature and oxygen partial pressure. From La_2O_3–MnO_x–ZrO_2 chemical potential diagram, lanthanum manganite and zirconia cannot coexist in equilibrium without $La_2Zr_2O_7$ formation at high temperatures (≥1000 °C) according to the reaction[34]

$${\rm LaMnO_3} + {\rm ZrO_2} \overset{k}{=} \frac{1}{2}{\rm La_2Zr_2O_7} + {\rm MnO}_x + \frac{3-x}{2}{\rm O_2} \tag{4}$$

The forward reaction rate (k) for the above reaction increases with decreasing PO_2 ($k \propto PO_2{}^{-((3-x)/2)}$) and formation of $La_2Zr_2O_7$ remains favorable in 10^{-6} atm PO_2. The $La_2Zr_2O_7$ phase field is asymmetric and according to defect cluster model, ZrO_2 excess $La_2Zr_2O_7$ is more stable than the stoichiometric and La_2O_3-excess $La_2Zr_2O_7$,[35] which is consistent with 2–7% excess lanthanum in YSZ regardless of sintering atmosphere (Tables 2 and 3).

For the samples sintered in 10^{-3} atm and 10^{-6} atm PO_2 followed by sintering in air, the quantity of $La_2Zr_2O_7$ is found to be significantly smaller compared to those sintered in 10^{-3} atm and 10^{-6} atm PO_2. This observation is also supported by the absence of $La_2Zr_2O_7$ phase in the XRD analysis. This indicates that the reaction products formed during sintering at lower oxygen pressures have the tendency to revert back to initial products according to the reaction:

$$\frac{1}{2}{\rm La_2Zr_2O_7} + \frac{1}{3}{\rm Mn_3O_4} + \frac{4}{3}{\rm O_2} = {\rm LaMnO_3} + {\rm ZrO_2} \tag{5}$$

The presence and co-stability of various phases in reactions (4) and (5) has been validated experimentally as described in Section 3.4.

5. Conclusions

The role of sintering atmosphere on the structural and chemical stability of $La_{0.8}Sr_{0.2}MnO_3$ (LSM)–8 mol.% yttrium stabilized zirconia (YSZ) composite has been studied as a function of oxygen partial pressure at 1400 °C. The LSM and YSZ preferentially react to form $La_2Zr_2O_7$ and Mn_3O_4 phases in sintering atmospheres containing lower oxygen pressures. For the samples initially sintered in reduced PO_2 atmospheres and resintered in air, these reaction products tend to revert back to the original starting material composition of LSM and YSZ. The unit cell volume of LSM increases with decreasing oxygen partial pressure because of changes in the manganese oxidation state.

Acknowledgments

This work was financially supported by US Department of Energy under a contract from Siemens Corporation – under the grant number 635383. Technical discussions with Dr. S.D. Vora, National Energy Technology Laboratory (NETL), Pittsburgh, is gratefully acknowledged.

References

1. *Fuel cell hand book*. 7th ed. Morgantown, WV: EG&G Technical Services, U.S. Department of Energy, Office of Fossil energy, National Energy Technology Laboratory; 2004.
2. Williams MC. Solid oxide fuel cells: fundamentals to systems. *Fuel Cells* 2007;**7**:78–85.
3. Jacobson AJ. Materials for solid oxide fuel cells. *Chem Mater* 2010;**22**:660–74.
4. Singh P, Minh NQ. Solid oxide fuel cells: technology status. *Int J Appl Ceram Tech* 2004;**1**:5–15.
5. Yokoo M, Tabata Y, Yoshida Y, Hayashi K, Nozaki Y, Nozawa K, et al. Highly efficient and durable anode-supported SOFC stack with internal manifold structure. *J Power Sources* 2008;**178**:59–63.
6. Mahapatra MK, Lu K. Glass-based seals for solid oxide fuel and electrolyzer cells – a review. *Mater Sci Eng* 2010;**67**:65–85.
7. Sun C, Hui R, Roller J. Cathode materials for solid oxide fuel cells: a review. *J Solid State Electrochem* 2010;**14**:1125–44.
8. Bongio EV, Black H, Raszewski FC, Edwards D, McConville CJ, Amarakoon VRW. Microstructural and high-temperature electrical characterization of $La_{1-x}Sr_xFeO_{3-\delta}$. *J Electroceram* 2005;**14**:193–8.
9. Petric A, Huang P, Tietz F. Evaluation of La–Sr–Co–Fe–O perovskites for solid oxide fuel cells and gas separation membranes. *Solid State Ionics* 2000;**135**:719–25.
10. Amesti AM, Larrañaga A, Martínez LMR, Aguayo AT, Pizarro JL, Nó ML, et al. Reactivity between $La(Sr)FeO_3$ cathode, doped CeO_2 interlayer and yttria-stabilized zirconia electrolyte for solid oxide fuel cell applications. *J Power Sources* 2008;**185**:401–10.
11. Tai LW, Nasrallah MM, Anderson HW, Sparlin DM, Sehlin SR. Structure and electrical properties of $La_{1-x}Sr_xCo_{1-y}Fe_yO_3$. Part 2. The system $La_{1-x}Sr_xCo_{0.2}Fe_{0.8}O_3$. *Solid State Ionics* 1995;**76**:273–83.
12. Hashimoto S, Fukuda Y, Kuhn M, Sato K, Yashiro K, Mizusaki J. Oxygen nonstoichiometry and thermo-chemical stability of $La_{0.6}Sr_{0.4}Co_{1-y}Fe_yO_{3-\delta}$ ($y = 0.2$, 0.4, 0.6, 0.8). *Solid State Ionics* 2010;**181**:1713–9.
13. Jiang SP. Development of lanthanum strontium manganite perovskite cathode materials for solid oxide fuel cells: a review. *J Mater Sci* 2008;**43**:6799–833.
14. Mizusaki J, Yonemura Y, Kamata H, Ohyama K, Mori N, Takai H, et al. Electronic conductivity, seebeck coefficient, defect and electronic structure of nonstoichiometric $La_{1-x}Sr_xMnO_3$. *Solid State Ionics* 2000;**132**:167–80.
15. Jiang SP. A comparison of O_2 reduction reactions on porous $(La,Sr)MnO_3$ and $(La,Sr)(Co,Fe)O_3$ electrodes. *Solid State Ionics* 2002;**146**:1–22.
16. Vohs JM, Gorte RJ. High-performance SOFC cathodes prepared by infiltration. *Adv Mater* 2009;**21**:943–56.
17. Mitterdorfer A, Gauckler LJ. $La_2Zr_2O_7$ formation and oxygen reduction kinetics of the $La_{0.85}Sr_{0.15}Mn_yO_3$,$O_2$ (g)/YSZ system. *Solid State Ionics* 1998;**111**:185–218.
18. Ricoult MB. Interface chemistry in LSM–YSZ composite SOFC cathodes. *Solid State Ionics* 2006;**177**:2195–200.
19. Poulsen FW, Puil NV. Phase relations and conductivity of Sr- and La-zirconates. *Solid State Ionics* 1992;**53–6**:777–83.
20. Stochoniol G, Syskakis E, Naoumidis A. Chemical compatibility between strontium-doped lanthanum manganite and yttria-stabilized zirconia. *J Am Ceram Soc* 1995;**78**:929–32.
21. Roosmalen JAM, Cordfunke EHP. Chemical reactivity and interdiffusion of $(La, Sr)MnO_3$ and $(Zr, Y)O_2$, solid oxide fuel cell cathode and electrolyte materials. *Solid State Ionics* 1992;**52**:303–12.
22. Chen M, Liu YL, Hagen A, Hendriksen PV, Poulsen FW. LSM–YSZ reactions in different atmospheres. *Fuel Cells* 2009;**9**:833–40.
23. Chen A, Bourne G, Siebein K, DeHoff R, Wachsman E, Jones K. Characterization of lanthanum zirconate formation at the A-site-deficient strontium-doped lanthanum manganite cathode/yttria-stabilized zirconia electrolyte interface of solid oxide fuel cells. *J Am Ceram Soc* 2008;**91**:2670–5.
24. Stevenson JW, Hallman PF, Armstrong TR, Chick LA. Sintering behavior of doped lanthanum and yttrium manganite. *J Am Ceram Soc* 1995;**78**:507–12.
25. Meixner DL, Cutler RA. Sintering and mechanical characteristics of lanthanum strontium manganite. *Solid State Ionics* 2002;**146**:273–84.
26. Wiik K, Schmidt CR, Falland S, Shamsili S, Einarsrud M, Grande T. Reactions between srtontium-substituted lanthanum manganite and yttria-stabilized zirconia: I. powder samples. *J Am Ceram Soc* 1999;**82**:721–8.
27. Virkar AV. A model for solid oxide fuel cell (SOFC) stack degradation. *J Power Sources* 2007;**172**:713–24.
28. Liu YL, Hagen A, Barfod R, Chen M, Wang HJ, Poulsen FW, et al. Microstructural studies on degradation of interface between LSM–YSZ cathode and YSZ electrolyte in SOFCs. *Solid State Ionics* 2009;**180**:1298–304.
29. Yang CCT, Wei WCJ, Roosen A. Reaction kinetics and mechanisms between $La_{0.65}Sr_{0.3}MnO_3$ and 8 mol.% yttria-stabilized zirconia. *J Am Ceram Soc* 2004;**87**:1110–6.
30. Palcut M, Wiik K, Grande T. Cation self-diffusion and nonstoichiometry of lanthanum manganite studied by diffusion couple measurements. *J Phys Chem C* 2007;**111**:813–22.
31. Rørmark L, Wiik K, Stølen S, Grande T. Oxygen stoichiometry and structural properties of $La_{1-x}A_xMnO_{3\pm\delta}$ ($A = Ca$ or Sr and $0 \leq x \leq 1$). *J Mater Chem* 2002;**12**:1058–67.
32. Kawashima T. Phase equilibria in ZrO_2–Y_2O_3–MnO_t ternary system at 1673 K. *Mater Trans* 1999;**40**:967–71.
33. Van Roosmalem JAM, Cordfunke EHP. A new defect model to describe the oxygen deficiency in perovskite-type oxides. *J Solid State Chem* 1991;**93**:212–9.
34. Chen M, Grundy AN, Hallstedt B, Gauckler LJ. Thermodynamic modeling of the La–Mn–Y–Zr–O system. *Calphad* 2006;**30**:489–500.
35. Stanek CR, Minervini L, Grimes RB. Nonstoichiometry in $A_2B_2O_7$ pyrochlores. *J Am Ceram Soc* 2002;**85**:2792–8.